Digital particle image velocimetry/thermometry and application to the wake of a heated circular cylinder

H. G. Park, D. Dabiri, M. Gharib

Abstract Digital particle image velocimetry/thermometry (DPIV/T) is a technique whereby the velocity and temperature fields are obtained using thermochromic liquid crystal (TLC) seeding particles in water. In this paper, the uncertainty levels associated with temperature and velocity measurements using DPIV/T are studied. The study shows that large uncertainties are encountered when the temperature is measured from individual TLC particles. Therefore, an averaging procedure is presented which can reduce the temperature uncertainties. The uncertainty is reduced by computing the average temperature of the particles within the common specified sampling window used for standard DPIV. Using this procedure, the velocity and temperature distributions of an unsteady wake behind a heated circular cylinder are measured experimentally at $Re = 610$. The instantaneous DPIV/T measurements are shown to be useful for computing statistical flow quantities, such as mean and velocity-temperature correlations.

List of symbols

B blue intensity
b normalized blue intensity
b_λ transmission of blue
C_p heat capacity
D diameter of cylinder
G green intensity
Gr   Grashof number ($[g\beta(T_c - T_\infty)D^3]/v^2$)
g normalized green intensity
$\boldsymbol{g}$ acceleration of gravity
g_λ transmission of green
H hue
I intensity
k thermal conductivity

L span of cylinder
P_λ spectrum of light source
p helical pitch of liquid crystal
$\dot{Q}$ heat input
$\dot{q}$ heat input per unit mass
R red intensity
R_λ reflectance of surface
Re   Reynolds number ($(U_\infty D)/v$)
r normalized red intensity
$\hat{r}$ orientation vector of liquid crystal
r_λ transmission of red
S saturation
T temperature
T_∞ freestream temperature
T_c surface temperature of cylinder
T_{tc} temperature of thermocouple inside cylinder
t time
U_∞ freestream velocity
u_i ith velocity component
v_1 first hue – saturation vector
v_2 second hue – saturation vector

Greek symbols

β coefficient of expansion
λ wavelength
ρ density
v kinematic viscosity
ω vorticity

1
Introduction

Digital particle image velocimetry/thermometry (DPIV/T) is a set of experimental techniques to measure simultaneously both velocity and temperature fields of a flow. The temperature is measured by seeding the flow with thermochromic liquid crystal (TLC) particles. These particles change their reflected wavelength as a function of temperature, and by calibrating reflected wavelength vs. temperature using a color CCD camera, the local temperature of the flow can be deduced. The velocity is measured by using the same particles as Lagrangian flow tracers. Using standard DPIV technique, the local velocity or displacement of the flow can be measured by cross-correlating local windows from two sequential images.

Several studies have been made using this technique to measure the velocity and temperature of a flow. Dabiri and Gharib (1991) measured a temperature distribution of a heated vortex ring, while Hiller et al. (1993) measured

H. G. Park
Jet Propulsion Laboratory, California Institute of Technology
Pasadena, CA 91109, USA

D. Dabiri, M. Gharib
Graduate Aeronautical Laboratories, California Institute
of Technology, Pasadena, CA 91125, USA

Correspondence to: H. G. Park

the velocity and temperature distribution of a natural convection in a cube. In this paper, the uncertainties associated with several different calibration methods are presented for measuring temperatures in water. While there have been studies of uncertainty levels for TLCs which are applied to surfaces (Camci et al. 1992; Farina et al. 1994; Hay and Hollingsworth 1996), there has been little documentation about the uncertainty levels when TLC particles are used to measure temperatures in liquids, namely water.

With uncertainties quantified, the DPIV/T technique is applied to measure the velocity and temperature distributions of the wake of a heated circular cylinder. From the instantaneous velocity-temperature data, it is demonstrated that DPIV/T can be used for statistical measurements of turbulent flows. While DPIV/T currently has lower spatial resolution and accuracy than traditional combination probe of hot-wire and cold-wire, DPIV/T has the advantage of being non-intrusive and may be a viable new method to measure velocity-temperature correlations.

2
Digital particle image velocimetry/thermometry

2.1
Thermochromic liquid crystals
A complete description of the thermochromic liquid crystals (TLCs) and their behavior can be found in Parsley (1991). To summarize, the TLCs are made up of long-chain organic molecules that can exist in either the smectic or the nematic phase. In the smectic phase, all the molecules are layered with long axes oriented (or oriented nearly) in one particular direction. In the nematic phase, the molecules are not layered, but the long axes of nearby molecules are still oriented nearly in one particular direction. If the molecules in the nematic phase are also chiral, i.e., the molecules are not symmetric about their long axis, the molecules become rotated slightly with respect to adjacent molecules forming a helical structure. This helical structure defines a pitch, p, which is the distance over which the molecules rotate 360 degrees. If a light of wavelength p hits this layer of TLCs, it is both transmitted and reflected. The component of the light which has circular polarization with the same hand sign as the helix direction is transmitted, while the other component of the opposite direction is reflected. All other wavelengths (in the visual range) are transmitted. Therefore, when white light is shone on chiral nematic TLCs, a light of only one particular wavelength is reflected. It is this property, along with the property that the pitch of the TLCs changes as a function of temperature, which allows the TLCs to be used to measure temperature by observing its reflected wavelength. Typically, the pitch changes inversely with temperature, hence, a sequence of colors from red, green, to blue will be observed as the temperature is increased.

The TLCs come in two packaged forms, raw mixtures and micro-encapsulated particles. In the micro-encapsulated form, the TLCs are sealed in polymer shells to form discrete particles. The size of the particles is controlled during manufacture and can range from 1 μm to nearly a millimeter. The advantage of micro-encapsulation is that the TLCs are protected from external contamination such as water. Thus micro-encapsulated TLC particles have a much longer life than unprotected raw TLC particles that are made by dicing raw TLC mixtures. The disadvantage of micro-encapsulation is that the light must pass through a polymer shell, which may distort the color and produce color variations from particle to particle. While raw TLC particles may have potential for better color consistency, the problems of contamination, degradation, and coalescence of particles are difficult to overcome, and only the characteristics of micro-encapsulated TLC particles are reported in this study. As a compromise, a batch of thin-shelled micro-encapsulated TLC particles (BM40C26W20) were custom manufactured by Hallcrest, Inc. The particles were manufactured with only minimal polymer material to produce very thin shells to maximize the consistency of reflected colors.

2.2
Calibration of thermochromic liquid crystals
To measure temperature with the TLCs, a calibration is needed between the reflected wavelength and the temperature. One possible method is to use an imaging spectrometer to measure the reflected light spectrum at every picture element. Unfortunately, imaging spectrometers are extremely expensive, are difficult to build, and require massive storage devices. The more sensible method is to use a camera with a limited number of spectral filters and infer the reflected wavelength by measuring the projections onto the spectral filters. The transmission characteristics of the spectral filters, therefore, form a set of basis vectors for a color space. For standard NTSC color cameras, three basis vectors, i.e., filters, whose transmission curves are given by r_λ, g_λ, and b_λ are used as shown in Fig. 1. The magnitude of the projections onto these basis vectors, R, G, and B, are given by:

$$R = \int_0^\infty R_\lambda P_\lambda r_\lambda \mathrm{d}\lambda \ ,$$

$$G = \int_0^\infty R_\lambda P_\lambda g_\lambda \mathrm{d}\lambda \ , \qquad (1)$$

$$B = \int_0^\infty R_\lambda P_\lambda b_\lambda \mathrm{d}\lambda$$

where R_λ is the spectral reflectance of an object, P_λ is the spectral power distribution of the light source, and λ is the wavelength. It is more convenient to work with normalized values of R, G, and B where:

$$r = \frac{R}{R + G + B}$$
$$g = \frac{G}{R + G + B} \qquad (2)$$
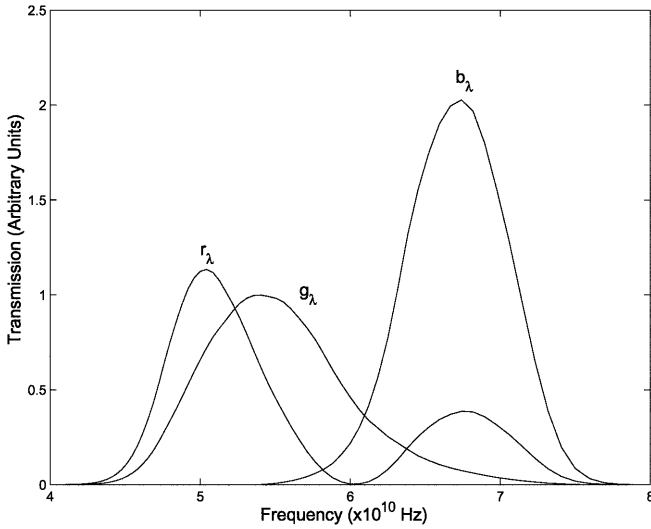$$b = \frac{B}{R + G + B}$$

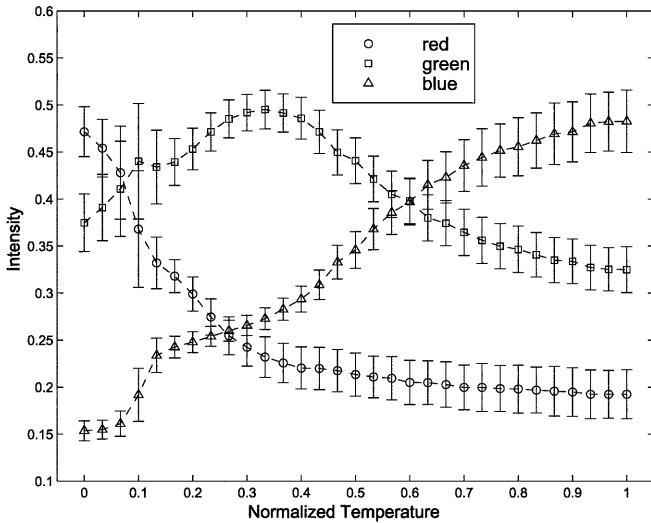**Fig. 1.** Transmission curves of NTSC color filters

Fig. 2. Curves of r, g, and b channels as function of temperature for TLC particles (Hallcrest BM40C26W20). The temperature is normalized by $(T - T_{min})/(T_{max} - T_{min})$, where $T_{min} = 25.8$ °C and $T_{max} = 28.5$ °C. The *bars* are the standard deviations of each color channel at a given temperature

For a monochromic reflecting object, the set of values of r g b is unique is simply the set of values of r_λ, g_λ, and b_λ at the given wavelength. If the reflected wavelength from the TLCs is monochromic or nearly so, a simple look-up table is sufficient to deduce the wavelength and hence the temperature. In practice, the reflected wavelength of the TLCs is not perfectly monochromic. Instead, there is a dominant wavelength and a distribution spread about this wavelength. If the spread is large and/or the reflected light is contaminated by other wavelengths, there is no guarantee that the set of r g b is unique. This is a drawback of having a limited set of filters instead of a large set of filters as in an imaging spectrometer. Fortunately, in most cases the sets of r g b of the reflected light from the TLCs are unique as a function of temperature, since there is a dominant wavelength for each temperature.

Having a unique function for the set of r g b for each temperature, it is possible to construct a temperature calibration curve. The most straightforward method is using the curves of r g b (or simply r and g, since $b = 1 - r - g$) as function of temperature, i.e., $T = f[g(r, g, b)]$. The typical calibration curves of r g b are plotted in Fig. 2. These r g b curves were used by Kimura et al. (1993) for training a neural-network. Unfortunately, there exist variations in the reflected wavelength from particle to particle at the same temperature. The cause is believed to be non-uniformity during the manufacture of the TLCs. This results in some scatter in the calibration.

The most popular calibration has been the hue variable (Dabiri and Gharib 1991; Camci et al. 1992; Behle et al. 1996; Hay and Hollingsworth 1996). The hue, H, comes from transforming R G B color space into H S I color space, or hue, saturation, and intensity, respectively. One possible transformation from R G B to H S I space is given by:

$$\begin{bmatrix} v_1 \\ v_2 \\ I \end{bmatrix} = \begin{bmatrix} 2/\sqrt{6} & -1/\sqrt{6} & -1/\sqrt{6} \\ 0 & 1/\sqrt{6} & -1/\sqrt{6} \\ 1/3 & 1/3 & 1/3 \end{bmatrix} \begin{bmatrix} R \\ G \\ B \end{bmatrix} \qquad (3)$$

$$H = \tan^{-1}(v_1/v_2) \qquad (4)$$

$$S = \sqrt{v_1^2 + v_2^2} \qquad (5)$$

The H S I color space relative to the R G B color space is shown in Fig. 3. The intensity variable, I, is the measure of the brightness of the light. The saturation, S, is the measure of the purity of the color. If the R, G, and B values lie close to the intensity vector, the light has low saturation or is nearly colorless since equal parts of R, G, and B is defined to be white. Away from the intensity vector, the light has high saturation or is nearly pure in color since there is little white component. Finally, the hue, H, is the measure of the color or the dominant wavelength of the light. Therefore, it is a most natural definition or variable for the temperature calibration of TLCs. The hue curve as function of temperature generated from r g b values in Fig. 2 is shown in Fig. 4.

The definition of the H S I space is not unique. Depending on the color basis vectors or the white (colorless) point, the transformation from R G B to H S I space may
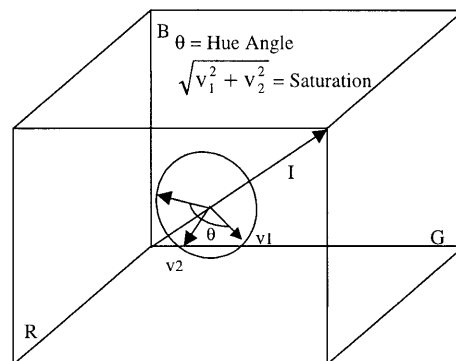

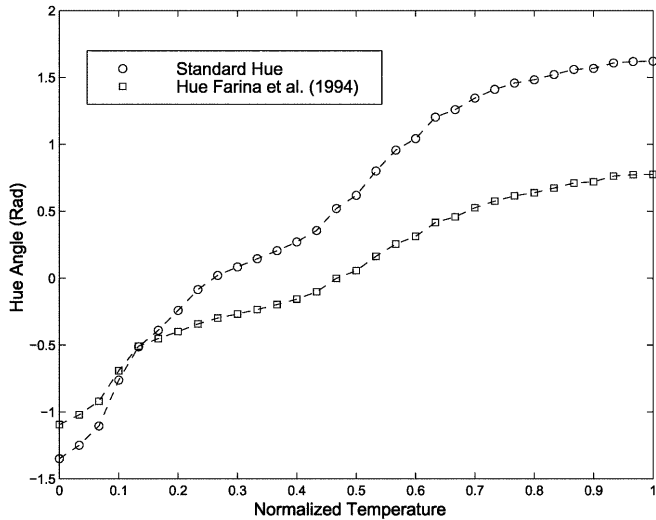**Fig. 3.** H S I color space in relation to R G B color space

Fig. 4. Standard hue and hue as defined by Farina et al. (1994) as function of temperature generated from *r g b* curves in Fig. 2

be different from Eq. (4). In formulating a definition for hue, there are some criteria that should be satisfied. Strictly speaking, hue should be insensitive to white light, i.e., insensitive to saturation. It can be seen in Eq. (4) that adding any constant to *R*, *G*, and *B* values on the right does not alter the value of hue, although the saturation, Eq. (5), is altered. Hue should also be insensitive to intensity, and it can been seen in Eq. (4) that multiplying *R*, *G*, and *B* values with any constant value does not alter the hue. In fact, there is an infinite number of definitions of hue which satisfy these criteria, and any angle between two independent vectors perpendicular to the intensity vector will satisfy. However, some authors (Farina et al. 1992; Hiller et al. 1993) have used alternate definitions. Farina et al. (1992), for example, have used:

$$\begin{bmatrix} v_1 \\ v_2 \\ I \end{bmatrix} = \begin{bmatrix} -1/4 & -1/4 & 1/2 \\ 1/4 & -1/2 & 0 \\ 1/3 & 1/3 & 1/3 \end{bmatrix} \begin{bmatrix} R \\ G \\ B \end{bmatrix} \quad (6)$$

$$H = \tan^{-1}(v_1^2 / v_2^2) \quad (7)$$

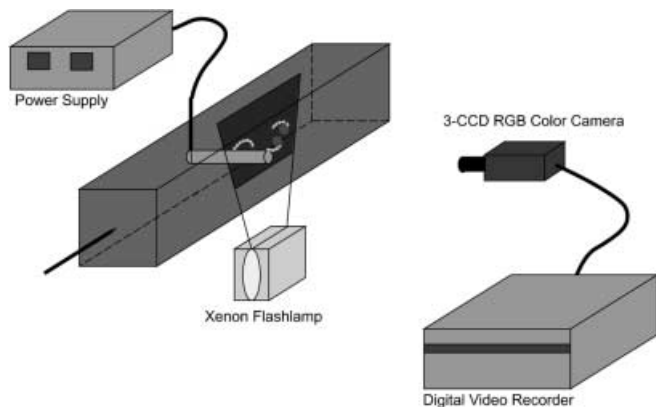$$S = \sqrt{v_1^2 + v_2^2} \quad (8)$$

Fig. 5. DPIV/T experimental setup

which do not satisfy the strict criteria of hue. The hue curve using this definition is also shown in Fig. 4. While not invariant to saturation, this alternate definition can work as well in generating a temperature calibration as shown in a later section.

3
Implementation

3.1
DPIV/T setup

The DPIV/T experimental setup is shown in Fig. 5. The test section was made of 1.27 cm thick clear Lucite and had an internal cross-sectional area of 15.2 cm by 15.2 cm. The tunnel operated at flow speeds between 3 and 50 cm/s. The flow was seeded with encapsulated TLC particles and was illuminated by a reflector assembly. The assembly produced a sheet of light at the center of the test section. The light reflector assembly consists of a mirror surfaced elliptical cylinder with a thin slit on top as shown in Fig. 6. The light is produced by two 25 cm long xenon flash-tubes located at the foci of the ellipse. The light escaping through the slit and was collimated by two lenses to form a light sheet of 2–3 mm thickness. Each flash-tube was fired at 15 Hz with a flash duration of 150 μs and an energy release of 8 J. The two flash-tubes were fired alternately to synchronize with the 30 Hz framing rate of the NTSC standard video camera. By alternately firing the two flash-tubes, synchronization with the 30 Hz framing rate of a NTSC standard video camera was achieved with sufficient power and cooling.

The flow was imaged from the side of the water tunnel using a 3-CCD color camera (Sony DXC-9000) which had a standard set of NTSC color filters. The *R*, *G*, and *B* color video signals were recorded on a real-time digital video recorder. The *R*, *G*, and *B* color channels from the camera were digitized to 24-bit color resolution (8–bits/channel)
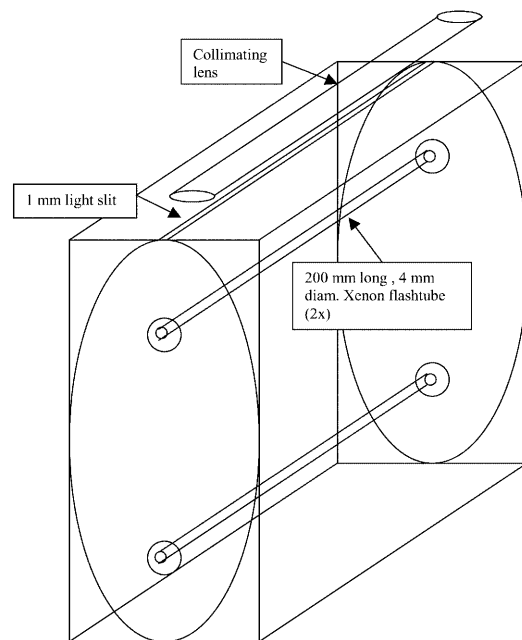

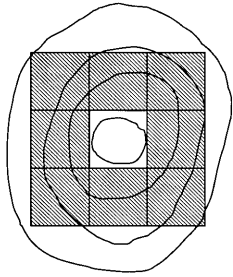**Fig. 6.** Elliptical xenon light reflector assembly

Fig. 7. Eight nearest neighboring pixels surrounding the centroid pixel

Fig. 8. Neural network configuration

using an analog-to-digital frame grabber (Coreco RGB-SE) to form 640×480 pixel *RGB* color images which were stored on to a hard disk array in real-time. Before digitization, the offset and the gains of the analog-to-digital converters were adjusted to maximize dynamic range and ensure that the dark current, i.e., pedestal, of each CCD was removed.

3.2
Data processing

The *R*, *G*, and *B* color channels from the camera are digitized to 24-bit color resolution (8–bits/channel) using an analog-to-digital frame grabber (Coreco RGB-SE) to form a 640×480 pixel *RGB* color image and stored directly to hard disk in real-time. Before digitization, the offset and the gains of the analog-to-digital converters were adjusted to ensure that the dark current, i.e., pedestal, of each CCD is removed and the dynamic range maximized.

The first step needed to measure the temperature is to locate the TLC particles and extract the color information. The TLC particles must be first located since the color information is contained only within them. To locate the particles, an intensity image, Img_1, was generated from the *RGB* color image. A second contrast enhanced image, Img_2, was created from Img_1, and a threshold operation was applied to Img_2 to create a list of particles. Then the precise centroid locations of each TLC particle were found by locating the intensity maximum in Img_1. The *r g b* values of each TLC particle were computed by conditionally averaging the centroid pixel and the eight pixels surrounding the centroid pixel as shown in Fig. 7. A conditional averaging procedure was used to reject *r g b* values from pixels that had low saturation levels, i.e., no color. This procedure has two benefits. First, the bright spots, i.e., regions of clipped signals, on a TLC particle, such as the ones near the particle centroid, do not skew the average. Second, dust or contamination particles, which are sometimes unavoidable in a water tunnel, are rejected because they are usually colorless and/or reflect much more intensely than TLC particles.

Once the average values of *R*, *G*, and *B* of each particle were determined, each particle was assigned a temperature using one of the calibration curves discussed in the previous temperature calibration section. The velocity field was computed by applying the standard DPIV cross-correlation technique (Willert and Gharib 1991) on a pair of intensity images. The interrogation window size was
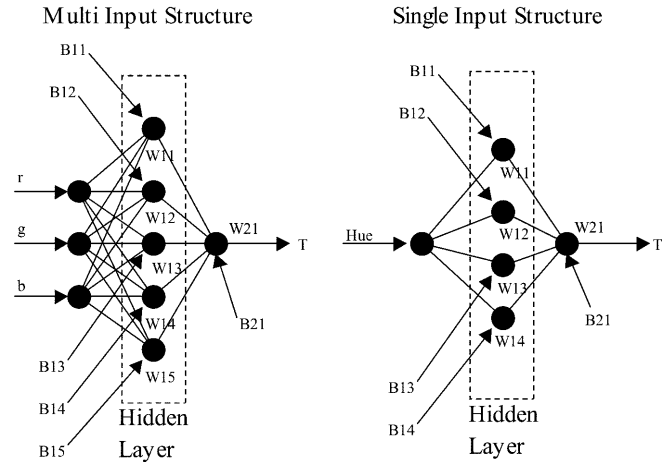
32×32 pixels with grid spacing of 8 pixels for window overlap of 75%.

3.3
Temperature calibration procedure

The calibration of the TLCs was made in-situ in the water tunnel facility prior or following the experiments. Because the reflected wavelength of TLCs is a function not only of temperature but also of viewing and illumination angles (Fergason 1968; Parsley 1991; Farina et al. 1994), the exact same viewing, illumination, and distance arrangements as the experiments must be maintained during the calibration. For the procedure, the tunnel was set to a constant speed, and the flow was seeded with micro-encapsulated TLC particles (Hallcrest BM40C26W20). These TLCs have a temperature range of 20 °C under the on-axis lighting arrangement, i.e., the same illumination and viewing angle. However, the useful range of these TLCs is reduced to about 2.5 °C, or a range from approximately 26 to 29 °C, when the 90° off-axis lighting arrangement is used as required for these experiments. Starting from the temperature of colorlessness of the TLC particles (<25 °C), the temperature of the tunnel was slowly increased. The water temperature was measured using a RTD temperature probe (Fluke 2180 A) which has a resolution of 0.01 °C. A set of images was taken at each temperature increment of 0.1 °C up to 30 °C.

3.4
Neural-network training

In this study, an artificial neural-network is used to fit the calibration data, similar to Kimura et al. (1993). The neural-network arrangements for single and multi-input networks are shown in Fig. 8. Four neurons in the hidden layers are used for a single input network and five neurons for a multi-input network. The networks were trained by using the mean calibration curves (Figs. 2 and 4) as training vectors and the measured temperatures as target vectors. Using the standard back-propagation technique, the weights and biases of each node (neuron) were adjusted until the root-mean sum of the difference between the actual and the evaluated values of the target vectors

from the set of training vectors is minimized. Typically, 1000 epochs or iterations were required to train the neural-network, and the quality of fit was excellent with a relative error of less than 0.05% through each target value in the temperature range.

3.5
Uncertainties

The largest uncertainty in the measured temperature of individual TLC particles comes from the non-uniformity in the manufacture of the TLC particles. Even under uniform temperature and lighting conditions, color variations between particles were observed. Since the TLCs are made from a complicated mixture of organic compounds, some variation may be expected in the chemical composition of the TLCs from particle to particle. For the micro-encapsulated TLC particles, another cause is a variation in the thickness of the polymer shell which can cause light refraction. Furthermore, the process of encapsulating the TLCs in a polymer shell may introduce residual stresses. These stresses can mechanically alter the helical pitch and change the color reflection properties of the TLCs.

The scatter in $r\,g\,b$ values of individual particles with all these effects is shown in Fig. 2. The scatter was computed from the standard deviations of $r\,g\,b$ values computed from 3,000 to 5,000 measurements, i.e., particle temperatures, for each temperature. The scatter translates into uncertainties in the measured temperature as shown in Fig. 9. The uncertainty using $r\,g\,b$ values vs. temperature varied from 5% at the middle temperature ranges to 20% at the extreme ranges. The uncertainty levels were higher for the calibration using $r\,g\,b$ values because the training of the multi-input neural-network covered less input variable space than a single input neural-network. The input variable space was greatly expanded when using multi-inputs, i.e., n^3, but the number of training vectors increased only slightly, i.e., $3n$. Thus the neural-network became trained for a very narrow set of input values, and when presented with input values with large scatter, the output became unpredictable.
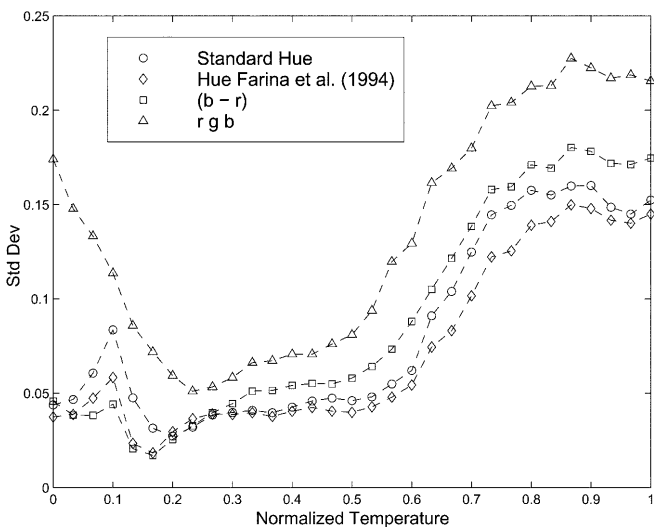
The uncertainty is significantly reduced using the hue calibration curves. The uncertainty falls from 5% at the middle temperature ranges and 20% at the extreme ranges to 4% and 15%, respectively. The two definitions of hue, either the standard or the one used by Farina et al. (1994), have similar uncertainty levels, although the hue used by Farina et al. (1994) appears slightly better. This result somewhat contradicts the findings of Hay and Hollingsworth (1996) who found that the standard hue definition has a lower uncertainty level than the one used by Farina et al. (1994). However, the difference in the uncertainty levels between the two definitions is not very significant in Hay and Hollingsworth (1996) and may depend on the types of TLC formulations and manufacture.

The uncertainty (5–20%) is too high to be acceptable and needs to be reduced for useful temperature measurements. Therefore, a spatial averaging procedure was introduced to reduce the uncertainty at a given $x - y$ location. Instead of simply reporting the temperature at a given location by that of the nearest particle, the temperature at any point in the image was computed by averaging the temperatures of particles that were inside a specified (32 × 32 pixel) window centered about the location. This averaging procedure was consistent with the technique of DPIV which computes the velocity, i.e. displacement, at any point by averaging the velocity of particles which lie within a specified window (Willert and Gharib 1991). Thus the velocity and temperature reported by DPIV/T at a given location are the average values of a set of particles within a common specified window. The temperature field was computed with the same window size and grid spacing of those of the velocity field. The resulting reduction of the temperature uncertainty using this averaging procedure with a 32 × 32 pixel window is shown in Fig. 10. The uncertainty was reduced to 2% at the middle ranges and to 8% at the extreme ranges. The price for this reduction in the uncertainty was a reduction in spatial resolution. However, this price is minimal since only the average velocity of the particles in the same specified window can be obtained using DPIV.
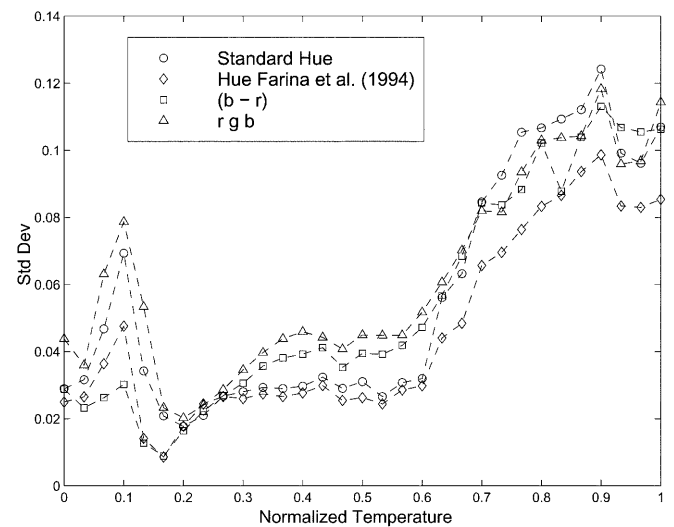

Fig. 9. Uncertainty in the computed temperature from individual particles

Fig. 10. Uncertainty in the computed temperature using 32 × 32 interrogation window

The accuracy error of the mean temperature, computed from a large number of individual measurements, was estimated to be on the order of 2%. The accuracy of the mean was determined by the shifts in the calibration curve. One cause of shift is the degradation of the TLC particles that occurs after several hours (>8 h) of exposure to water. During the experiments, the TLC particles were stabilized in water for an hour or so and were then flushed after a few hours (~6 h). The TLC particles could be used only for a limited time if accurate mean temperature was desired. The shift in the calibration curve after a day of exposure to water is shown in Fig. 11.

The uncertainty in the velocity in a specified window using DPIV is of the order of 1% (Willert and Gharib 1991). The accuracy error in the mean velocity is estimated to be of the order of 1%. The combined uncertainty in the velocity–temperature correlation ($u_i'T'$) for individual 32×32 pixel window is 3–10%, and the accuracy error of the correlation is estimated to be about 3%. A list of the uncertainty levels in DPIV/T, as well as the accuracy levels, is presented in Table 1.

4
Application of DPIV/T to wake behind a heated circular cylinder

4.1
Experimental setup/conditions
The flow chosen to apply DPIV/T is the wake behind a heated circular cylinder at Re = 610 and Pr = 6. At this Reynolds number, the wake is unsteady and turbulent. The experiment was carried out in the same facility as described in the previous section on the DPIV/T setup. The freestream temperature, T_∞, and the velocity, U_∞, were 25.8 °C and 6.4 cm/s, respectively. The cylinder was heated with a constant power input of 63.8 W. The test cylinder was an electrically heated rod (Watlow Firerod) of diameter, $D = 9.53$ mm. A J-type thermocouple that measured the cylinder temperature was embedded in the
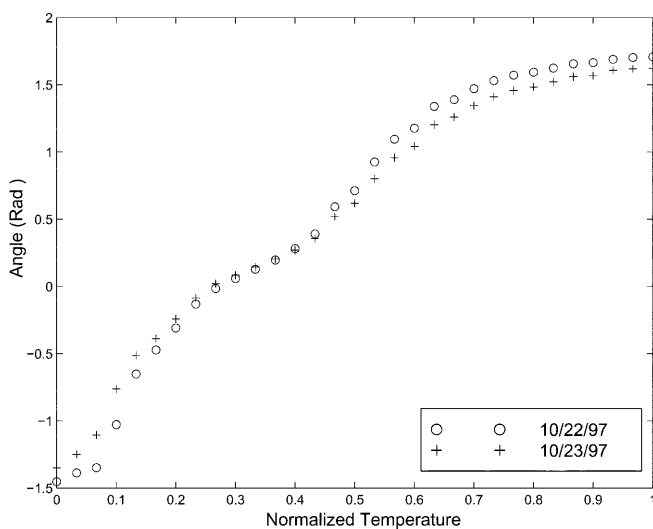
Table 1. Uncertainty levels in DPIV/T

	Uncertainty of individual particle	Uncertainty using 32×32 pixel sampling window	Error in accuracy
Velocity	N/A	1%	1%
Temperature	5–20%	2–10%	2%
Velocity–temperature correlation	N/A	3–10%	3%

core of the cylinder at mid-span. The temperature was measured by a thermocouple thermometer (Omega HH21) that had a temperature resolution of ±0.1 °C. The cylinder was heated by a constant DC voltage power supply (Kepco BOP 50–4M) that maintained a thermal boundary condition of constant integrated heat flux over the surface of the cylinder. The temperature at the core of the cylinder, T_{tc}, was 41.5 °C, and the estimated temperature at the surface of the cylinder, T_c, was 36.8 °C. The ratio between the Grashof number and the square of the Reynolds number, Gr/Re^2, which is a measure of the buoyancy effect, was low enough (0.01) to not affect the wake structure.

The cylinder was mounted horizontally by two vertical hollow supports at the ends of the cylinder. The electrical and thermocouple leads from the cylinder passed through the hollow supports to the power supply and thermocouple thermometer, respectively. The supports were thermally insulated from the cylinder by a layer of silicone rubber. The disturbance to the flow by the supports was minimized by placing the supports outside of two flat end plates with rounded leading edges. The distance between the two end plates was 12.1 cm, and thus the effective aspect ratio   (L/D) of the cylinder was 13. Further details of this setup can be found in Park (1998).

The camera was placed approximately 2 m from the test section and imaged an area of 60 mm wide by 50 mm high at the mid-span of the test section. The flow was seeded with 40 μmm diameter thin-walled encapsulated (custom made) TLC particles (Hallcrest BM40C26W20) that have a thermal response time of 4 ms (Dabiri and Gharib 1991). The response time was much smaller than the expected time scale of the vortex shedding ($\approx$600 ms). The flow was illuminated from the bottom of the test section by a xenon white light sheet as described in a previous section, and the images were digitized to a real-time digital video recorder with 8-bit resolution per RGB channel (24-bit total).

4.2
Instantaneous measurements
An instantaneous view of the flow with the heated cylinder in place is shown in Fig. 12. The derived temperature and velocity fields using DPIV/T are shown in Fig. 13. The temperature field was generated from the standard hue calibration curve. Although the standard hue does not appear to do as well as the hue defined by Farina et al. (1994) in reducing the uncertainties, the standard hue is believed to be more robust since it is invariant to satura-
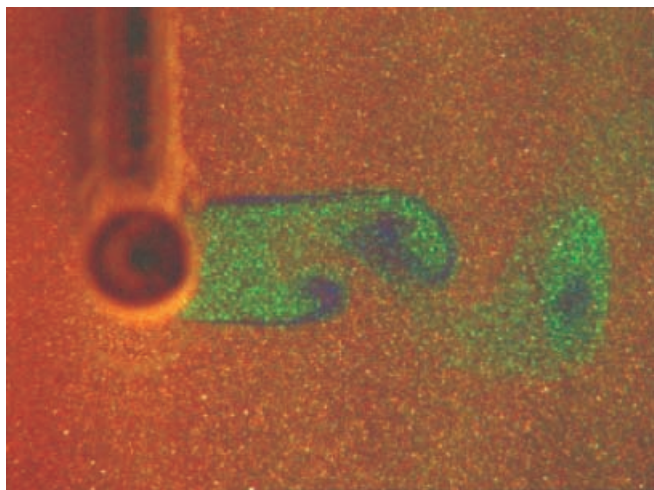

Fig. 11. Shift in the calibration curve (standard hue) after one day of exposure to water

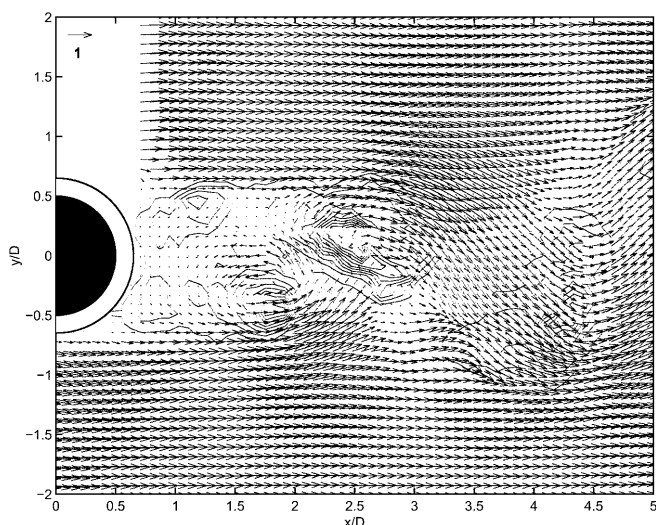**Fig. 12.** Instantaneous view of the flow behind a heated circular cylinder

Fig. 13. Velocity and temperature fields computed using DPIV/T from image in Fig. 12 (temperature, $(T - T_\infty)/(T_c - T_\infty) > 0.01$, contour increment 0.01; velocity, u/U_∞)

tion. This is an important consideration because changes in the seeding density, which occurs during the course of the experiment when heavier TLC particles settle to the bottom of the tunnel, can change the mean saturation level of the images. The standard hue also has very low and flat uncertainties in the normalized temperature range of 0.2–0.6 where most of the temperature measurements reside. For these reasons, the standard hue was chosen.

Figure 13 outlines some limitations of the experimental setup. First, the setup is such that the supports prevent any gathering of information about the velocity or the temperature above the cylinder. Also, the immediate area surrounding the cylinder (shown by the larger white concentric circle outside the cylinder in Fig. 13) cannot be imaged due to light blockage by the end of the cylinder nearest to the camera. Figure 13 also shows the spatial limitation of DPIV/T. DPIV/T cannot resolve the boundary layer, so no information can be obtained about the tem-

perature distribution near the cylinder surface. Again because current implementation of DPIV/T uses 32×32 pixel interrogation windows ($0.3D \times 0.3D$), the thin thermal shear layers ($\approx 0.1D$) visible in Fig. 12, were not resolved. However, once the scales of the flow reached the order of the cylinder diameter when the shear layers rolled-up ($x/D > 2.5$), reliable temperature measurements are possible using DPIV/T. This resolution limitation of DPIV/T is further discussed in a later section.

5
Statistical measurements

5.1
Mean results
The mean values were computed from 1,000 instantaneous measurements, and the mean velocity field is shown in Fig. 14. The mean temperature field and the profiles of temperature at $x/D = 1$, 2, 3, and 4 are shown in Figs. 15 and 16, respectively. The standard deviations of the mean (SDOMs) of the profiles are shown as the light error bars. The SDOM is the uncertainty associated with the unsteady fluctuations of the flow, not the measurement uncertainty of DPIV/T. The temperatures at the thin shear layers were greatly underestimated at $x/D = 1$ because of the resolution limitation of DPIV/T.

The mean global turbulent heat flux, $\overline{u_j' T'}$, can be computed from this data set as shown in Fig. 17 which shows that the structure of $\overline{u_j' T'}$ in the near wake is dominated by two large counter-rotating vortex-like structures ($x/D \approx 2$, $y/D \approx \pm 0.5$), symmetric about the wake centerline.

5.2
Phase averaged results
Examples of the phase averaged vorticity, $\langle \omega_z \rangle$, and temperature $\langle T \rangle$ are shown in Figs. 18 and 19, respectively. The average at each phase was computed by subdividing the time between consecutive zero crossings of the u_y
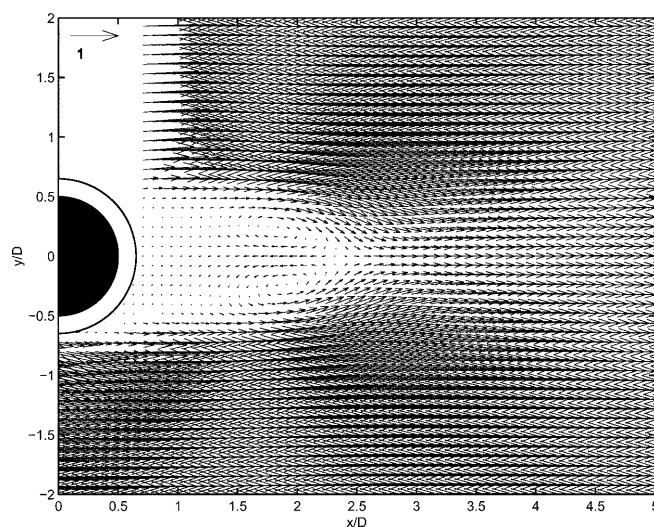

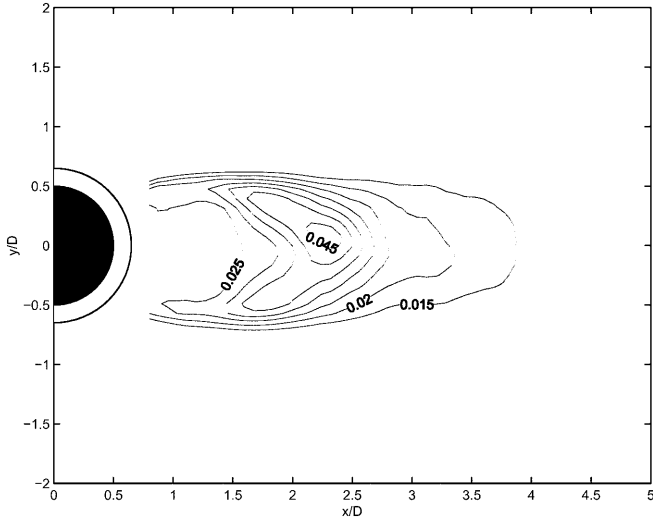**Fig. 14.** Mean velocity field of stationary cylinder at Re = 610 (normalization: u/U_∞)

Fig. 15. Mean temperature field of stationary cylinder at Re = 610 [normalization: $(T - T_\infty)/(T_c - T_\infty)$]
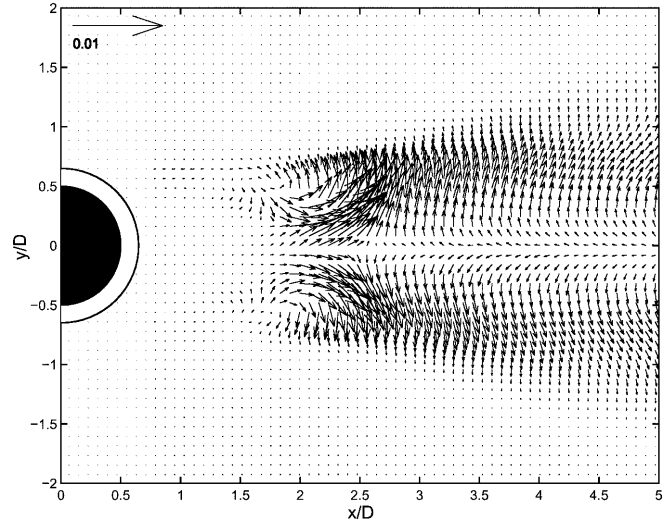

Fig. 17. Mean global turbulent heat flux of stationary cylinder at Re = 610 [normalization: $u_j' T'/U_\infty (T_c - T_\infty)$]
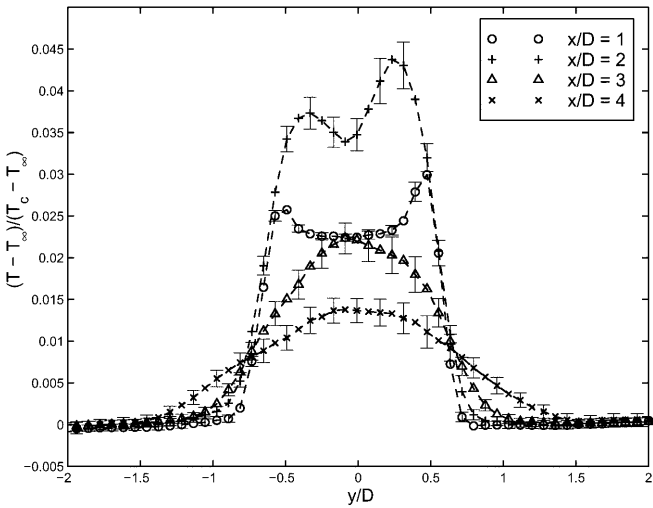
Fig. 16. Mean temperature profiles at various downstream locations at Re = 610. The *error bars* indicate standard deviation of the mean
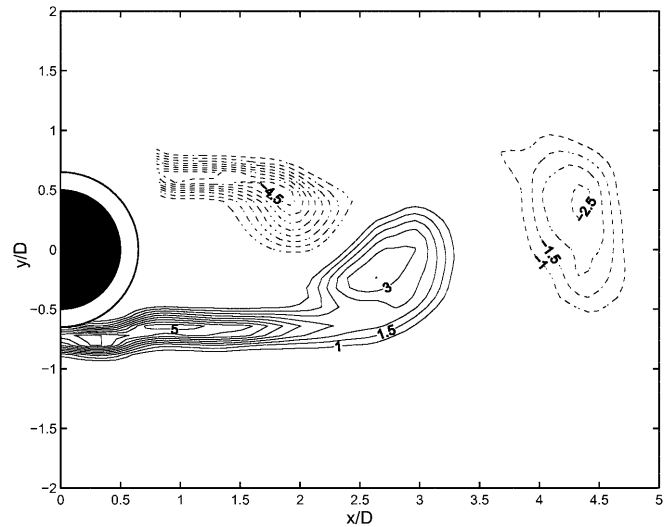

Fig. 18. Phase averaged vorticity field for stationary cylinder at Re = 610 ($|\langle \omega_z \rangle D/U_\infty| > 1.0$, contour increment 0.5)

signal into 12 evenly spaced phases using roughly 80 vortex shedding cycles. Because the vortices roll-up from the hot shear layers, the temperature appears to be as good of a marker for the vortices as the vorticity. The phase averaged coherent (periodic) heat flux, $\tilde{u}_j \tilde{T}$, and the incoherent heat flux, $\langle u_{rj}' T_r' \rangle$, are shown in Figs. 20 and 21. The phase averaged coherent heat flux $\tilde{u}_j \tilde{T}$ is the periodic component of $\overline{u_j' T'}$, while the incoherent heat flux, $\langle u_j' T' \rangle$, is the fluctuating component of $\tilde{u}_j \tilde{T}$.

5.3
Resolved scales and data consistency

The described implementation of DPIV/T sacrifices spatial resolution for better temperature precision. Because the sampling window size is large ($0.3D \times 0.3D$), it is important to determine what scales are resolved and not resolved in the wake of the heated circular cylinder. The large-scale dynamics are captured well by DPIV/T since the local in-

tegral scale, l, becomes larger than D once the vortices are formed. However, prior to the roll-up of the vortices, the scale of the shear layers, which are laminar at Re = 610, is relatively small. An estimate of the thickness of the thermal shear layer using Blausis solution is $0.1D$ ($0.3D$ for momentum thickness) one diameter downstream of the cylinder. DPIV/T should resolve the velocity profile of the shear layer but the temperature profile may be under-resolved with a sampling window size of $0.3D$ by $0.3D$. This suspicion is confirmed by Fig. 22, which shows the plot of the total heat flux (sum of mean and turbulent heat flux) in the streamwise direction taken at each downstream location. The shear layers are indeed under-resolved, and the peaks at $y/D = \pm 0.6$ for $x/D = 1$ corresponding to the heat flux at the shear layers are neither sharp nor tall. The total heat flux (integral of the curve) at this downstream location is much smaller as compared to locations farther downstream ($x/D = 2, 3, 4$).
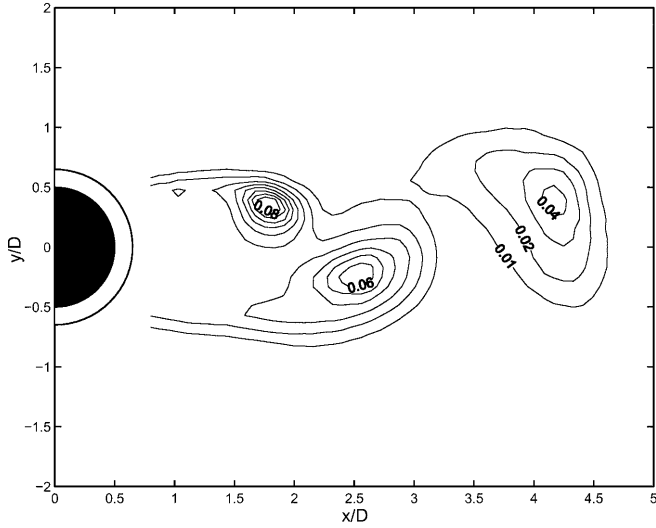
Fig. 19. Phase averaged temperature field for stationary cylinder at Re = 610 [$(\langle T \rangle - T_\infty)/(T_c - T_\infty) > 0.01$, contour increment 0.01]
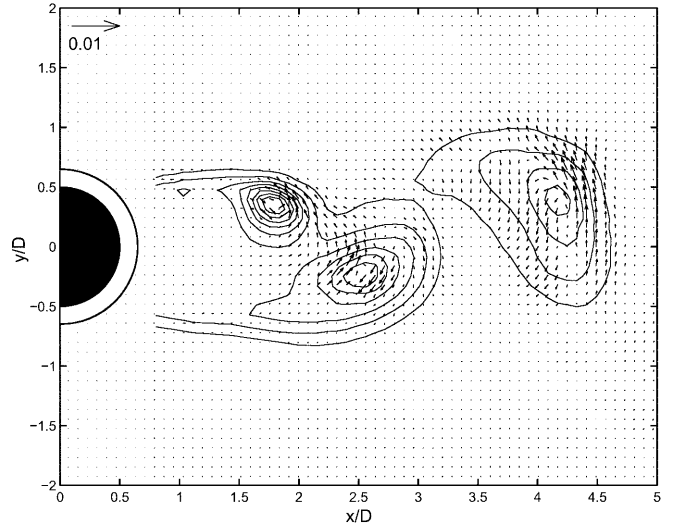

Fig. 21. Phase averaged incoherent heat flux for stationary cylinder at Re = 610 [Normalization: $\langle u'_{ri}T'_r \rangle / U_\infty(T_c - T_\infty)$]. The *solid lines* are contours of temperature $(\langle T - T_\infty \rangle)/(T_c - T_\infty) > 0.01$, contour increment 0.01)

Fig. 20. Phase averaged coherent heat flux for stationary cylinder at Re = 610 [normalization: $\langle u'_j T' \rangle / U_\infty(T_c - T_\infty)$]. The *solid lines* are contours of temperature $(\langle T - T_\infty \rangle)/(T_c - T_\infty) > 0.01$, contour increment 0.01)
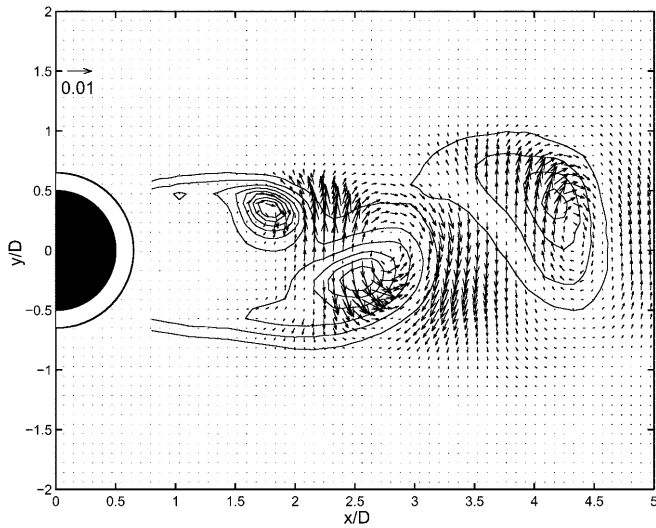

Fig. 22. Profiles of the total heat flux for different downstream locations

While DPIV/T has trouble resolving the shear layer, it does capture most of the energy of the velocity and temperature fluctuations once the vortices roll-up, and the scales of the flow become of the order D. A good test whether DPIV/T is capturing all of the energy associated with velocity and temperature fluctuations is to compute the total heat flux using DPIV/T for various downstream locations. The total heat flux can be measured using a wake survey method (Park 1998). The heat release of the cylinder, Q, can be computed by:

$$pC_pL \int_{-\infty}^{\infty} \left[\bar{u}_x(\bar{T} - T_\infty) + \overline{u'_x T'} - k\frac{\partial \bar{T}}{\partial x} \right] dy = Q \qquad (9)$$
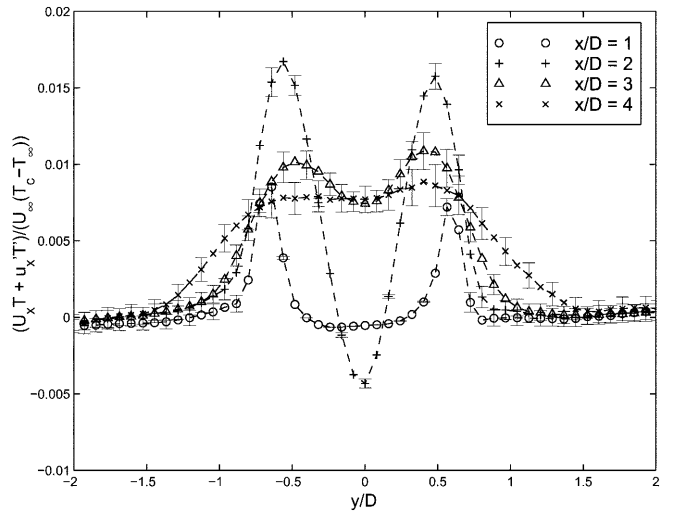
The computed results at downstream stations are shown in Fig. 23. The total heat flux should be ideally equal to the total heat released by the cylinder if the mean heat flux, $\bar{u}_x\bar{T}$ and the turbulent heat flux, $\overline{u'_x T'}$ are well resolved and computed accurately. For $x/D < 2$, the computed heat release by the cylinder is well below 63.8 W. This is because DPIV/T is unable to resolve the thin shear layers and capture all of the heat flux in the wake. Once the shear layers roll-up into the vortices ($x/D \approx 2$), DPIV/T is able to capture most if not all of the heat flux in the wake. For $x/D > 2$, the computed heat release becomes equal to or greater than the actual heat released by the cylinder. This discrepancy cannot be fully accounted for by the SDOM (standard deviation of mean) that is shown as the error bar. The SDOM is the uncertainty in the mean associated with the fluctuation generated by the vortex shedding. There are two possible reasons for this
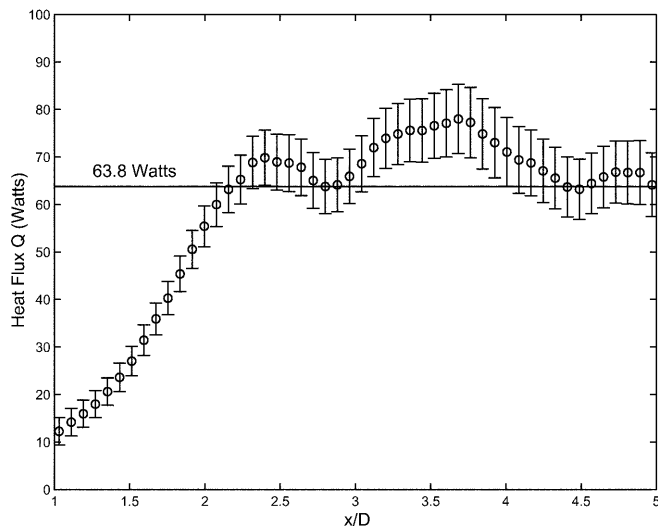
Fig. 23. Integral of the total heat flux for different downstream locations

discrepancy. One reason is that the flow is not strictly two-dimensional as assumed in computing the heat release of the cylinder in Eq. (9). If the cylinder or the wake has any spanwise variation in the heat flux, the computed heat release will be inaccurate since heat flux measurements from only one mid-span plane were used for the computation. The other reason is that the temperature measurements of DPIV/T are not accurate enough. The accuracy uncertainty of the temperature from DPIV/T measurements is estimated to be 2%. In actual temperature units, this corresponds to accuracy error of ±0.05 °C for a temperature span of 2.5 °C. The method of computing heat release using a wake survey of the heat flux turns out to be very sensitive to temperature uncertainty because the mean temperature in the wake is very low. While the instantaneous temperatures are large due to the formation of hot vortices, the mean temperature of the wake is very low. In fact, an accuracy error of ±0.02 °C, which is half of the estimated accuracy error of DPIV/T, fully accounts for the observed discrepancy. Thus the overestimation of the heat release by the cylinder is likely to be a combination of the inaccuracy of DPIV/T and a spanwise variation in the heat release by the cylinder. In conclusion, if the flow scales are resolved, DPIV/T can reliably measure velocity and temperature measurements with suitable uncertainty.

6
Conclusion
By using TLC particles as Lagrangian flow tracers, it is possible to measure simultaneously both the local velocity and the temperature of the flow. By generating a sheet of white light and capturing the images on to a 3-CCD color video camera, the velocity and temperature of the flow can be deduced from the displacement and the color of the TLC particles, respectively. A comprehensive study of the uncertainties involved in using the micro-encapsulated TLC particles for temperature measurement in water shows that there exists a large uncertainty (5–20%) in the

temperature measurement of individual TLC particles regardless of the temperature calibration method. It is found that the uncertainty can be reduced to 2–10% computed by averaging the temperatures of the particles within a specified sampling window used for standard DPIV. The accuracy errors of the mean temperature and mean velocity–temperature correlation ($u'_i T'$) using this temperature averaged DPIV/T are estimated to be 2% and 3%, respectively.

DPIV/T is then used to measure velocity and temperature distributions of the wake of a heated circular cylinder at $Re = 610$. In addition to instantaneous measurements, statistical flow measurements are made, such as the mean velocity-temperature and velocity–temperature correlations. The experiment demonstrates that DPIV/T can be a viable method to measure accurately velocity and temperature in turbulent flows.

6.1
Recommendations and future research
There are two important issues of DPIV/T which need to be addressed in the future. The first is the spatial resolution. This needs to be improved for study of turbulent flows. The simplest solution is to reduce the sampling window size from 32×32 to 16×16 pixels, but this can result in an unacceptable increase in the measurement uncertainty. A better solution would be to use a higher resolution camera. While imaging a smaller spatial area, a high-resolution camera can image more particles to maintain an acceptable level of uncertainty using a 32×32 pixel window size.

The second issue is the temperature (color) uncertainty in the TLC particles. Even under uniform temperature, the particles exhibit color variations. The variation is thought to come from non-uniformity during the manufacture of the TLCs as well as the process of micro-encapsulation can introduce residual stresses which can affect the color by physically changing the pitch length of the TLCs. Micro-encapsulated TLC particles also have polymer shells which can cause optical distortion. Therefore, unencapsulated (raw) TLC particles have the potential for better color consistency, and preliminary experiments demonstrate this. However, the problems of contamination, degradation, and coalescence of the particles are difficult to overcome and need to be addressed further.

References
Behle M; Schulz K; Leiner W; Fiebig M (1996) Color-based image processing to measure local temperature distributions by wideband liquid crystal thermography. Appl Sci Res 56: 113–143

Camci C; Kim K; Hippensteele SA (1992) A new hue capturing technique for the quantitative interpretation of liquid crystal images used in convective heat transfer studies. J Turbomach 114: 765–775

Dabiri D; Gharib M (1991) Digital particle image thermometry: the method and implementation. Exp Fluids 11: 77–86

Farina DJ; Hacker JM; Moffat RJ; Eaton JK (1994) Illuminant invariant calibration of thermochromic liquid crystals. Exp Thermal Fluid Sci 9: 1–12

Fergason JL (1968) Liquid crystals in nondestructive testing. Appl Opt 7: 1729–1737

Hay JL; Hollingsworth DK (1996) A comparison of trichromic systems for use in the calibration of polymer-dispersed thermochromic liquid crystals. Exp Thermal Fluid Sci 12: 1–12

Hiller WJ; Koch ST; Kowalewski TA; Stella F (1993) Onset of natural convection in a cube. Int J Heat Mass Transfer 36: 3251–3263

Kimura I; Kuroe Y; Ozawa M (1993) Application of neural networks to quantitative flow visualization. J Flow Visual Image Process 1: 261–269

Parsley M (1991) The Hallcrest handbook of thermochromic liquid crystal technology. Hallcrest, Glenview, Ill

Park HG (1998) A study of heat transport processes in the wake of a stationary and oscillating circular cylinder using digital particle image velocimetry/thermometry. PhD thesis, California Institute of Technology, Pasadena, Calif

Willert CE; Gharib M (1991) Digital particle image velocimetry. Exp Fluids 10: 181–193